TOTAL CURRENT SPECTROSCOPY

S.A. KOMOLOV

Research Institute for Physics, Leningrad State University, Ul. 1 May-100, Leningrad, Petrodvorets, U.S.S.R.

and

L.T. CHADDERTON *

Physics Laboratory II, H.C. Ørsted Institute, Universitetsparken 5, DK-2100 Copenhagen, Denmark

In total current spectroscopy (TCS) a beam of low energy (0–15 eV) electrons is directed upon a solid sample and secondary electron emission investigated by monitoring the current to the target, rather than by direct energy analysis of emitted electrons. A TCS signal is the derivative of the direct current with respect to the incident energy E_1, displayed as a function of that energy, and obtained experimentally in ultra high vacuum conditions using simple modulation and lock in amplification techniques. A typical experimental arrangement is described and factors influencing a typical spectrum outlined. A simple background theory is discussed and it is shown how TCS is a powerful tool for studying not only the surface and near surface regions, but also bulk physics. In particular the technique has already found application in studies of work function, chemi- and physisorption, epitaxy, interband transitions, densities of states, excitons, impurity atom excitation, plasmons, radiation damage and the measurement of thicknesses of very thin surface layers.

1. Introduction

The first lecture in an undergraduate course on surface physics often begins with the lecturer drawing a horizontal line on the board, writing "solid" below the line, and "vacuum", (or "gas", or "plasma") above it. In subsequent development of the often complicated experimental methods used in surface physics the idealization of that horizontal line — the surface — is frequently forgotten. The truth is that while we know much about solids, and about both gases and plasmas, our knowledge of the surface region is presently rather poor. Furthermore the surface of a real solid is never abrupt. Both atomic and electronic properties of the solid — be it amorphous *or* crystalline — merge with those of the surrounding gas or plasma in a way which is quite complicated, and over finite distances. Real surfaces also

---

* Now at CSIRO, Division of Chemical Physics, P.O. Box 160, Clayton, Victoria, Australia 3168.

possess defects which form a separate study, quite independent of those defects in the solid which themselves terminate at the surface.

Many of the experimental methods used to study surfaces are sophisticated but, at least in the case of methods using electron or ion beams, are relatively harsh in that the analysing beam itself perturbs the surface under investigation — simply because the energy is high. Thus the ion beam used in Rutherford backscattering studies (RBS) can displace atoms at and below the surface, even in the modification of the technique employing inclined beams [1], whilst Auger Electron Spectroscopy (AES) has as its very basis the energy analysis of electrons ejected from rather deep levels.

To the many experimental spectroscopies employing electrons may be added another which we call Total (or Target) Current Spectroscopy (TCS). The beauty of this technique lies in its simplicity and in the fact that it employs electron beams at very low energies, typically in the range 0—15 eV, so that it is of a gentle probing nature. In spite of this low energy TCS reveals information not only about the surface (defined as the first two atomic layers) and near surface (defined as the first five atomic layers) regions, but also about the bulk of the solid itself. Depth information is therefore incorporated in the experimental spectral display. It will become clear that, in addition to studies of fundamental physics, TCS can also be used as a tool of investigation for applied problems, for example corrosion, oxidation, physisorption, chemisorption, adhesion, and very low energy radiation damage.

As with any technique TCS has limitations. One of these is that it gives no information regarding the surface *arrangements* of atoms or molecules, but only about distributions of a statistical nature. However, TCS can readily be incorporated in conventional LEED systems if the appropriate energy modifications can be made. Secondly TCS is still so much in its infancy that there is no readily applicable detailed theory accounting for elastic and inelastic electron/electron interactions, and for interplay between these two processes. Nevertheless these drawbacks are either of a technical or a temporal nature and employment of TCS with other techniques will increasingly occur.

2. Experimental aspects of total current spectroscopy

The basis of the TCS technique is simple perpendicular incidence of a narrow beam of electrons onto the sample. For single crystals the range of electron energies employed can be made sufficiently low that emergence of the first order nonspecular LEED diffracted beams is avoided. In more than one sense, therefore, TCS can be considered complementary to both LEED and APS. It should also be noted that future development of TCS will see the employment of angular dependent studies.

Fig. 1 is a simple summary of what TCS comprises. A beam of electrons with

Electrons

$(E_1 = 0 - 15 \, eV)$

$J_2(E_1)$

$J_1(E_1)$

$J(E_1)$ X
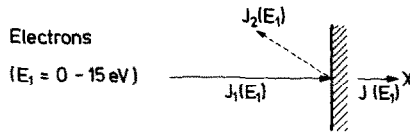
Total Current $= J(E_1) = J_1(E_1) - J_2(E_1)$

TCS is: $\boxed{S(E_1) = \dfrac{dJ(E_1)}{dE_1}}$

Required ?

   a) Ultra High Vacuum.
   b) Simple modulation and
      lock in amplification technique.

Fig. 1. Total current spectroscopy (TCS).

energies E_1 in the range 0—15 eV is directed onto a clean sample, which can be either single or polycrystalline. An electron gun of rather ordinary design is perfectly adequate for TCS, provided that the primary electron energy is varied by changing the potential in the sample circuit, so that the primary beam current is independent of the energy E_1. Traditionally the reflection of low energy electron beams from the surfaces of solids has been investigated by monitoring the reflected current $J_2(E_1)$ as a function of primary energy. For clean surfaces, fine structure in the resulting spectra is then a consequence of both elastic *and* inelastic electron/solid interactions. Primary features in the elastic reflection can correspond directly to the band structure above the vacuum level [2,3]. Secondary features can be attributed to the energizing of various fundamental excitations in the solid [4,5]. Structure in the inelastic reflection component is mainly due to characteristic energy losses [6,7]. In TCS, however, it is the current $J(E_1)$ carried by the *target* which is monitored. Since the total electron current in the target circuit is directly defined as the difference between the primary and secondary currents (fig. 1),

$$J(E_1) = J_1(E_1) - J_2(E_1), \tag{1}$$

all features in the energy dependence of the total (target) current are determined by corresponding inverse features in the secondary current.

A TCS curve is defined as the first derivative of the target current with respect to the incident energy:

$$S(E_1) = dJ(E_1)/dE_1, \tag{2}$$

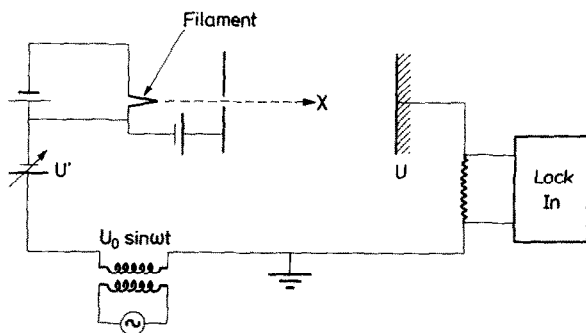displayed as a function of that energy. Since the electron energies are low it is clear

Fig. 2. Schematic illustration of the electronic circuit used in total current spectroscopy.

that "clean" samples can only be studied in ultra high vacuum conditions, and it is often necessary to desorb residual gas by heating the target in situ. Experimentally $S(E_1)$ is obtained using simple modulation and lock-in amplification techniques [8,9]. The halfwidth of the primary electron distribution is 0.5 eV, the energy being modulated at 430 Hz, 0.15 eV pp. A schematic illustration of the circuit is shown in fig. 2.

TCS is closely related to the familiar appearance and disappearance potential spectroscopies [10] and, in simple background theory [11], to electron energy loss, secondary electron emission and photoemission spectroscopies. It differs, however, in two important respects. Firstly, interest is centred on that very low energy region which is less accessible in other techniques. Secondly $S(E_1)$ is displayed as a function of increasing energy, beginning at $E_1 = 0$. This means that the low energy part of the spectrum is not in general influenced by higher energy loss processes which in some other methods, energy loss spectroscopy for example, take place simultaneously. Transitions can therefore be followed from their onset at some low energy threshold.

3. Theoretical aspects of the technique

3.1. Construction of the signal

We assume that the velocity distribution of electrons emerging from the gun filament along the x-axis (figs. 1 and 2) is $P(v_x) \, dv_x$ so that the flux is $v_x P(v_x) \, dv_x$. The primary current directed at the target is then given by:

$$J_1(v_1) = k \int v_x P(v_x) \, dv_x \, , \qquad (3)$$
$$(v_x + v_1) > 0$$

where k is a constant. For a sample potential U and a contact potential difference between sample and cathode U' (fig. 2) the primary energy E_1 can be defined as

follows:

$$E_1 = \tfrac{1}{2}mv_1^2 = e(U + U') \,, \tag{4}$$

and the velocity distribution recast as an energy distribution $N(W) = P(v_x)$, where:

$$W = \text{sign}(v_x) \times \tfrac{1}{2}mv_x^2 \,, \tag{5}$$

so that eq. (3) becomes:

$$J_1(E_1) = k \int\limits_{-E_1}^{\infty} N(W)\,\mathrm{d}W \,. \tag{6}$$

A corresponding expression for the secondary electron current,

$$J_2(E_1) = k \int\limits_{-E_1}^{\infty} N(W)\,R(W + E_1)\,\mathrm{d}W \,, \tag{7}$$

involves the total secondary electron emission coefficient $R(E)$, which includes all electron interactions — elastic and inelastic — between primary beam and solid. Here, then, lies the basic physics of the TCS technique. It follows, from eqs. (1), (6), (7) and (2) that:

$$S(E_1) = k \left\{ N(-E_1)[1 - R(0)] - \int\limits_{-E_1}^{\infty} N(W)\,\frac{\mathrm{d}R(W + E_1)}{\mathrm{d}E_1}\,\mathrm{d}W \right\} \,. \tag{8}$$

We examine this expression by referring to an idealized and schematic TCS curve (fig. 3). The first term in eq. (8) is proportional to the electron energy distribution in the primary flow; a peak is obtained in a typical spectrum corresponding to the contact potential difference between the cathode and the sample surface. Normally the position of this *surface peak* — which in some senses can be compared with the surface peak in channelling/RBS studies — is chosen as origin for the primary electron energy, and any energy change in the "surface potential" U is revealed by a shift of the energy distribution on the potential scale (abscissa). The surface potential is essentially the vacuum level. The second term in eq. (8), being dependent on the energy variations of $R(E)$, gives rise to fine structure — peaks and troughs — in the main body of the experimental spectrum, and is precisely the term containing detailed information on the fundamental electron–solid interaction.

It is worthwhile emphasizing again that TCS involves those interaction processes which alter the secondary electron current. The energy dependence of the elastic reflection coefficient clearly appears in TCS curves, but electron escape after inelastic scattering is also observed. In addition, features deriving from primary electron excitation of the solid (excitons, plasma oscillations, excitation of transfer states of the lattice or impurity atoms) — whilst not directly altering the secondary current — can be present. Conversely, in certain circumstances the energizing of
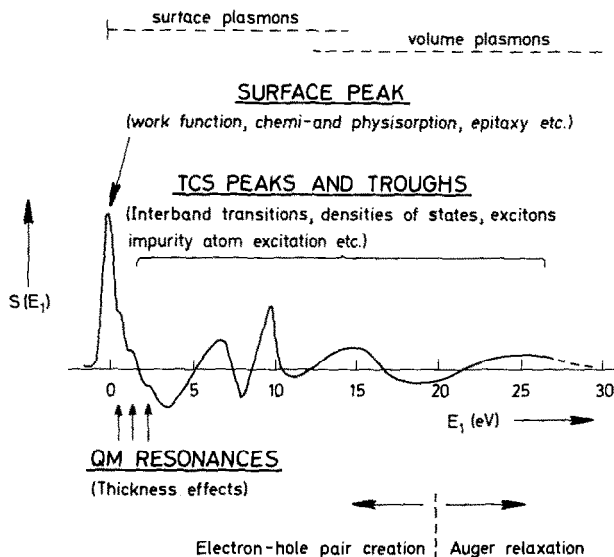
Fig. 3. An idealized and schematic total current spectrum.

these excitations may indeed change the probability of reflection from the solid. The energy thresholds of the excitations then correspond to definite features in the TCS curve.

In general low energy primary electrons may suffer *inelastic* scattering in the following processes [12]:

(i) electron—electron scattering leading to electron—hole pair production via the screened Coulomb interaction with valence electrons;

(ii) collective electron excitations — surface and bulk plasmons;

(iii) interaction with the lattice via electron/phonon scattering.

Processes (i) and (ii) are those most responsible for peaks and troughs [13] in a TCS spectrum, since Auger relaxation effects typically appear at somewhat higher energies. Surface plasmon scattering is more probable than volume plasmon scattering (fig. 3) if the mean depth of escape [14] is less than about 2.5 mm, which is certainly the case for metals and semiconductors. Coupling with plasmons, moreover, is less predominant in all but the nearly-free-electron-like metals. Pair production is therefore the major inelastic scattering mechanism to be accounted for at energies $E_1 < 50$ eV. These general remarks are substantiated in detail by a recent secondary electron emission study, and an associated theoretical analysis of the final density of states distribution in graphite [12].

We will indicate a procedure for calculating the total current spectrum in the case where we are involved with only interband transitions in a small band gap semiconductor, and with no other resonance process. Whilst stressing the oversimplified nature of this first order theoretical approach it will nonetheless later

become clear (section 4.4) that a comparison of theory with experiment is rather satisfactory. It is assumed that the electron/phonon scattering processes — or excitation of thermal vibrations with energy losses <100 meV — are those giving rise to *elastic* reflection. Such processes can be discussed in terms of an elastic mean free path L_1 which, for the energy interval 0–10 eV and for a variety of solids, has values >1–2 nm changing smoothly with energy [15]. *Inelastic* interactions in the same energy interval will then be associated with inelastic scattering accompanied by interband transitions.

In a random k approximation where the interband transition matrix elements are held constant [16,17] the inelastic mean free path L_2 becomes:

$$L_2(E_1) = v/W_{in} = [W_0 \int_0^\infty N_C(E) \int_{-\infty}^0 N_V(E_0) N_C(E_0 + E_1 - E) \, dE_0 \, dE]^{-1} v \,, \qquad (9)$$

where W_{in} is the inelastic scattering probability, W_0 a constant, v the electron velocity, and N_C and N_V are the density of states functions for the conduction and valence bands respectively. The primary electron energy E_1, the energy E after scattering and the energy E_0 of the excited electron in the valence band all are here, *measured from the bottom of the conduction band*. It is implicit in eq. (9) that the magnitude of L_2 is a consequence of detailed structure in the density of state distributions for the conduction and valence bands. A composite mean free path can then be defined as follows:

$$L(E_1) = L_1 L_2/(L_1 + L_2) \,. \qquad (10)$$

In order to account for those primary electrons having a momentum component perpendicular to the surface following scattering, and which can escape from the solid, we consider a primary flow n_0 directed at right angles to the sample surface. Attenuation gives a flow at a depth x of:

$$n(E_1, x) = n_0 \exp[-x/L(E_1)] \,. \qquad (11)$$

The number of electrons elastically scattered in an elemental slab of width dx at depth x is then proportional to the electron flow and to the reciprocal of the elastic mean free path:

$$dn(E_1, x) = (n_0/L_1) \exp[-x/L(E_1)] \, dx \,. \qquad (12)$$

Assuming isotropic scattering, and by defining a surface threshold function $C(E)$ [18], the flow of elastically reflected electrons is readily shown to be given by:

$$n_e(E_1) = \tfrac{1}{2} n_0 C(E_1) L(E_1)/L_1(E_1) \,. \qquad (13)$$

In order to account for the contribution of inelastic scattering to the reflected current it is necessary to proceed in two stages, since the energy E of the scattered electron is, of course, less than that of the primary (E_1). The first step therefore, is a calculation of the probability of scattering into the energy state E_1. This is fol-

lowed by a calculation of the probability of electron escape, the integration being carried out with respect to the energy above the vacuum level. The analytical expression for the inelastic component is then:

$$
n_{in}(E_1) = \tfrac{1}{2} n_0 L(E_1) \int_{E_V}^{\infty} \frac{C(E)\, L(E)}{L(E) + L(E_1)} \frac{W_0}{V} N_C(E)
$$

$$
\times \int_{-\infty}^{0} N_V(E_0)\, N_C(E_0 + E_1 - E)\, dE_0\, dE \ . \tag{14}
$$

For a comparison with experimental total current spectra it is then required that the signal be constructed from the following expression:

$$
S(E_1) = S(E_1)_e + S(E_1)_{in} \simeq -[dn_e/dE_1 + dn_{in}/dE_1] \ . \tag{15}
$$

3.2. The surface and near-surface regions

The significance of the surface peak (fig. 3) is twofold. First, for "clean" samples the position of the surface peak on the energy axis can be used in accurate determinations of the work function. For the theoretical background to this aspect of TCS the reader is referred to the work of Strayer, Mackie and Swanson [19]. The usual procedure is to make an in situ evaporation of a metal with a well known work function (e.g. silver) for comparative purposes (see section 4.1), in which case it is possible to measure the work function of the material under investigation to accuracies $\sim \pm 5$ meV.

Secondly, changes ΔU in the surface potential as revealed by shifts in the surface peak yield information about processes taking place *at* the surface. There is not space here to discuss the detailed theory of the many physical effects measurable in this way but it is obvious that outdiffusion of impurity atoms, adsorption and desorption of gaseous species (less than a monolayer), and evaporation of very small amounts of material onto the surface can be examined in this manner. A *sharp shift in the surface potential and therefore in the work function has also been* observed at the Curie point for clean nickel single crystals [20] — TCS can thus also be used for looking at solid state transitions as reflected by changes of surface properties.

Possibly a potentially more attractive application of the technique is in near-surface studies. Suppose that there exists a rather sharp transition in the near-surface region — as for example if there is an adsorbed layer of gas between 1 and 2 nm thick. There then appear quantum mechanical resonances in the TCS signal at very low energies (see fig. 3). With care it is possible to extract the background fundamental differential yield [13] and to pinpoint rather accurately the positions of the resonances on the energy scale.

The existence of such additional subsurface peaks can be explained on the basis
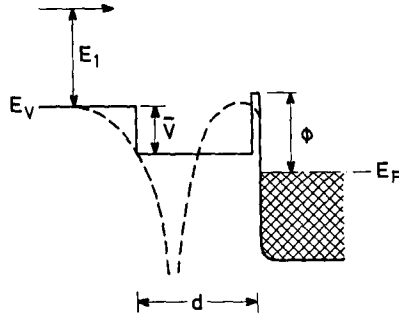
Fig. 4. Schematic potential diagram (stippled curve) for an adsorbed gas layer, and simplified model for same (heavy drawn). The model is characterized by an average potential $\bar{V}$ and a layer thickness d. E_V is the vacuum level, ϕ the work function, and E_F the Fermi level.

of a simple one-dimensional model of electron resonance transmission [21–23]. The model is characterized by two interfaces — the vacuum/layer and the layer/substrate interfaces — separated by a distance d corresponding to the layer thickness, and by an average layer potential $\bar{V}$ (fig. 4). Multiple electron scattering is described in terms of separable scattering properties for the two interfaces; a substrate coefficient of reflection R_1, and a vacuum/layer interface coefficient of reflection R_2. Summing over all forward and backward scattered electron waves we obtain [20], for the cases $R_1 R_2 \ll 1$, an expression for the transmission coefficient:

$$T(R_1, R_2) = (1 - R_1)(1 - R_2)[1 + 2(R_1 R_2)^{1/2} \cos 2\phi] , \tag{16}$$

where

$$\phi = (2m/\hbar) d(E_1 + \bar{V})^{1/2} = \alpha(E_1 + \bar{V})^{1/2} , \tag{17}$$

and $\alpha = 0.513d$, where d is in Å and energies are in eV.

In TCS, however, we are interested in the derivative:

$$\frac{dT}{dE_1} = - \frac{\alpha}{2(E_1 + \bar{V})^{1/2}} (1 - R_1) \times 4(R_1 R_2)^{1/2} \sin 2\phi \, (1 - R_2) . \tag{18}$$

for which maxima occur if:

$$2\phi = 2\pi n - \tfrac{1}{2}\pi , \tag{19}$$

or

$$\phi_n = (n - \tfrac{1}{4}) \pi , \quad n = 0, 1, 2, \dots . \tag{20}$$

The corresponding energy $E_1^{(n)}$ associated with each resonance number is, for eq. (17), then given by:

$$E_1^{(n)} = (\pi/\alpha)^2 (n - \tfrac{1}{4})^2 - \bar{V} . \tag{21}$$

For a given spectrum (at a given temperature) therefore, the resonance energy is a linear function of $(n - \frac{1}{4})^2$ with negative intercept $\bar{V}$. Accordingly, providing internal selfconsistency can be demonstrated for the values assigned to n (as for example by recording TCS curves at different temperatures for the case of gas adsorption and observed resonance shifts) it is possible to determine both $\bar{V}$ and d [13]. It should be clearly noted, however, that these are mean values and that the analysis is confined to the sharp limitations of the model (fig. 4.).

4. Some selected TCS investigations

4.1. Desorption and adsorption of gas on {100} vanadium

In this section we shall briefly discuss some selected investigations in which TCS has been used as a primary tool, beginning with a study of vanadium surfaces. For further details, particularly regarding sample preparation and detailed interpretation the reader should consult the original publications [13,14].

In the case of vanadium [13] thermal desorption of residual gas from the sample surface was followed by recording TCS curves during target heating. Throughout the entire cleaning process changes in the surface potential were carefully monitored and, in the temperature range 20–800°C, surface potential measurements only made on the hot sample after complete cessation of potential drift. Between 800 and 1500°C flash heating was employed with a flash duration of 5 min. The systematic changes in surface potential thus obtained are displayed in fig. 5.

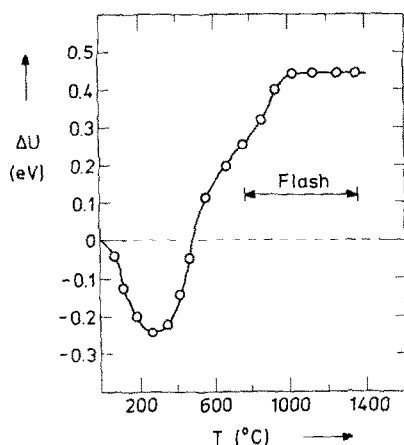Typical TCS curves corresponding to ascending sample temperatures during ther-

Fig. 5. Graph showing change of surface potential of {100} vanadium during thermal desorption.
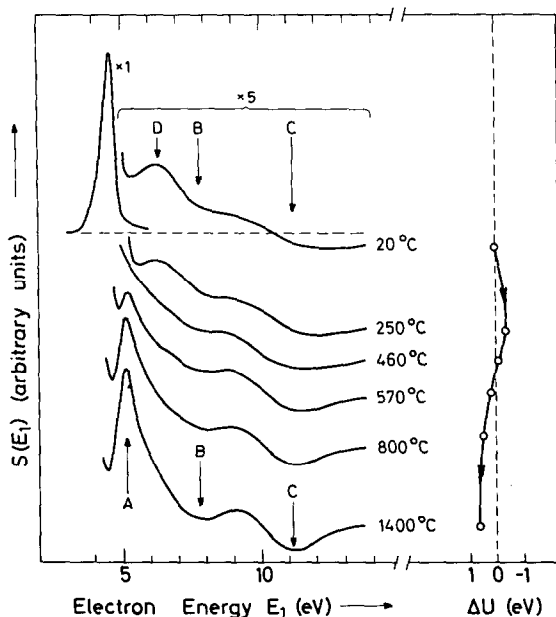
Fig. 6. Total current spectra from {100} vanadium at selected temperatures during thermal desorption. Peak D disappears whilst peak A and troughs B and C become prominent. The primary electron energy distribution is shown only for the first (20°C) spectrum; and the energy origin coincides with the Fermi level. Changes ΔU in the surface potential are displayed on the right hand side of the figure.

mal desorption studies are shown in fig. 6. The curves have their energy origin adjusted on the abscissa so as to coincide with the Fermi level of vanadium. Peaks at A and D correspond to increasing current $J(E_1)$, and the troughs at B and C to falling values of $J(E_1)$. The peak A appears only after heating to a temperature of 550°C, its amplitude apparently reaching a maximum when the vanadium surface is "clean". Also the energy location of A does not change with respect to the Fermi level during the heating process. Conversely the troughs B and C, which also become more pronounced, do move with respect to the Fermi level – their lateral displacement following the displacement of the surface potential. Accordingly it is their energy levels ($E_C = 3.8$ eV, $E_D = 7.3$ eV) with respect to the *vacuum* level which do not change. The peak D is strongest at the lower temperatures, before appreciable desorption of gas has taken place.

The surface potential movements of fig. 5 are interpreted [13] as being a consequence of the progressive desorption of gas with rising temperature. The fact that fig. 5 is not reversible on cooling – the surface potential shift returns smoothly to zero without passing through negative values – suggests that the adsorption process differs from desorption, and that there must be at least two species of gas pres-

ent with different binding energies and different signs of dipole moment. We pro-
pose that for $T < 300°C$ one species is relatively easily desorbed, and that we are
concerned with physisorption. In the higher temperature regime, $300 < T <
1000°C$, either strong physisorption takes place or chemisorption, in which a
change of electron affinity could give rise to the observed shifts. In view of the well
known influence of oxygen on vanadium surfaces we suggest that the species here
is chemisorbed oxygen. Oxidation of vanadium surfaces is in fact accompanied by
an increase in the work function [24].

We have been able to determine a value for the work function itself by in situ
evaporation of a silver film onto "clean" vanadium. Combining the value obtained
for the contact potential difference between vanadium and silver (0.52 eV) with a
published [25] work function for silver (4.47 eV), yields a value of $\phi_V = 3.95$ eV
for {200} vanadium. This agrees well with other work [26].

Peak A in the TCS curve (fig. 6) is clearly fundamental to vanadium, although
we are unable to give an explanation as to its origin. Troughs B and C, however,
can immediately be attributed to two thresholds in the secondary electron current
associated with ionization losses in vanadium. It has been shown previously [27]
that the bottom of the vanadium valence band (3–4 eV below the Fermi level) and
the maximum of the valence density of states (0.6–1.6 eV below the Fermi level)
are regions of high transition probabilities. Interband transitions are expected be-
tween these two zones and a region with a high density of empty states at ~3–3.5
eV above the Fermi level. Primary electrons can escape into vacuum from the
vanadium provided that the kinetic energy E_1 exceeds the energy lost in energizing
transitions, and it is electron escape which gives rise to observable thresholds in
TCS curves. Accordingly B and C can reliably be associated with interband transi-
tions at 3.8 and 7.3 eV rather than with elastic scattering resonances observed in
similar experiments with nickel [28].

The strong peak D of fig. 6 is the first of several quantal resonances of the kind
described in section 3.2, and is a consequence of the residual adsorbed gas layer
[13].

4.2. Epitaxy

Experiments on the epitaxial growth of gold and silver films on vanadium
substrates have also been performed [14]. A known mass of the metal was evapo-
rated onto the unheated vanadium from a hot filament at a specified distance, and
TCS measurements made simultaneously. In this way a slow transfer from features
characteristic of vanadium to features characteristic of the noble metal was ob-
served. Changes ΔU in the surface potential U are shown in fig. 7, as a function of
thickness d, for both Ag and Au. In each case the net work function increases dur-
ing film formation (compare fig. 5); ΔU saturates at about $d = 15$ Å for Ag and
$d = 30$ Å for Au. For the TCS curves themselves, for both Ag and Au, attenuation
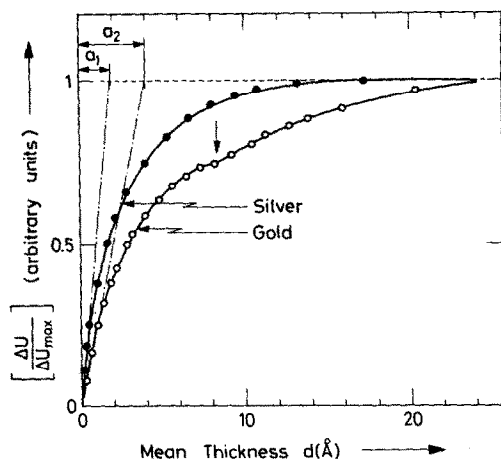of vanadium features is followed by the appearance of noble metal features at

Fig. 7. Graph showing the change of surface potential ΔU as a function of the mean thickness d of evaporated gold and silver layers on {100}vanadium.

$d \sim 6\text{–}8$ Å, and vanadium characteristics totally disappear for mean thicknesses $d \gtrsim 15$ Å.

Attenutation of the substrate signal can be understood in terms of simple additional scattering in the overlayer. Consider the thickness-dependent attenuation of the characteristic vanadium trough C in fig. 6 [14]. Primary scattering in the deposited film gives rise to an attenuation of intensity which, in a first approximation, can be expressed by the coefficient $\exp(-d/l_1)$, where d is again the mean film thickness and l_1 the primary electron mean free path. Now with respect to the Fermi level of vanadium the trough C lies at an energy $\simeq 12$ eV. Therefore electrons which subscribe to this characteristic feature must be able to travel back through the film and emerge with an energy just above the vacuum level. For the coefficient of attenuation of the secondary electrons we accordingly write $\exp(-d/l_2)$, where l_2 is the mean free path for electrons with an energy $\simeq 5$ eV. The total attenuation of intensity for both primary and secondary paths then becomes:

$$I(d) = I(0) \exp[-d(l_1^{-1} + l_2^{-1})] . \tag{22}$$

The experimentally determined dependence of the intensity of trough C on thickness, after extraction of background, is shown in fig. 8 for both Ag and Au. For mean thicknesses exceeding a certain minimum ($d_{Ag} \sim 2$ Å, $d_{Au} \sim 5$ Å) an inverse exponential relation corresponding to eq. (22) is observed. Values for a composite mean free path λ obtained from the slope

$$-\lambda^{-1} = -(l_2 + l_1)/(l_1 l_2)$$

are $\lambda_{Ag} \simeq 13$ Å and $\lambda_{Au} \simeq 55$ Å, in satisfactory agreement with results obtained
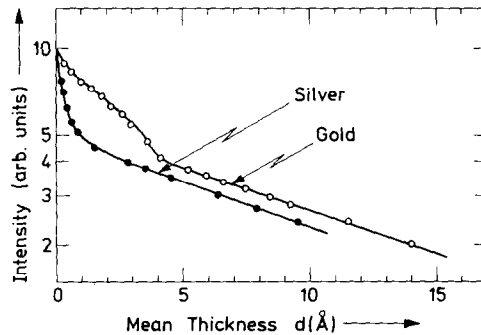
Fig. 8. Graph showing the attenuation of the "intensity" of a characteristic vanadium feature (C in figs. 2 and 3) as a function of the increasing mean thickness d of the evaporated overlayer. For both gold and silver there are clear nucleation and growth stages.

by other methods [29,30]. For example the mean free path values given by Kanter [29] (table 1) yield $\lambda_{Ag} \simeq 12$ Å and $\lambda_{Au} \simeq 13.5$ Å.

The anomalous attenuation of intensity seen in fig. 8 for small values of d must certainly be due to the nucleation stage of film growth, the exponential law being strictly valid only for a continuous homogeneous layer. For an island structure of small randomly oriented nuclei [31] the *average* thickness d of the overlayer is related to the percentage coverage θ by:

$$\theta = d/a , \tag{23}$$

where a is a critical nucleus size [32]. If we now ignore a small second order influence of island size on net work function [33], and assume a linear relationship between coverage and change of surface potential ΔU, we can make some estimate of the critical nucleus sizes for Ag and Au on vanadium. Thus, extrapolated straight lines from the primary portions of the experimental curves in fig. 7 give $a_1 \simeq 2$ Å for Ag and $a_2 \simeq 4$ Å for Au. Using a rotating dynamic capacitor technique Mitchinson and Pringle [32] find $a \simeq 2$ Å for Ag evaporated onto Au and $a \simeq 9$ Å for Au onto Ag, whilst Gretz [34] reports $a \simeq 2$ Å for Ag onto tungsten.

We conclude that the anomalous attenuation of intensity for the vanadium feature C takes place during the nucleation stage of film formation, when there are

Table 1
Electron mean free paths l in silver and gold

E (eV)	Ag (Å)	Au (Å)
6	36	45
10	18	19

many small nuclei whose size is much smaller than the internuclear distance. The initial rapid fall in intensity must accordingly be due to a fundamental change in the electron scattering properties of the vanadium surface coupled with a patch-field effect, rather than to scattering in the islands themselves. For thicknesses greater than the critical nucleus size, however, the signal attenuation follows the form expected, and is evidently due to electron scattering in the overlayer. The slight dip (arrowed) in the gold curve of fig. 7 occurs at a mean thickness d at which nucleation has ceased [31], and may well be associated with coalescence of overlayer nuclei.

4.3. Radiation damage in dysprosium ion implanted nickel

There is a growing interest in the creation of amorphous metallic systems by ion implantation. In the case of the Dy/Ni system the interest lies in the resultant magnetic properties. Alloys of such rare earth and ferromagnetic materials are conventionally prepared by evaporation onto liquid-nitrogen-cooled substrates (splat cooling) [20]. Ion implantation offers an attractive experimental alternative for production of amorphous alloys, and TCS an alternative technique for studying the alloy itself and its recovery during annealing. For a detailed description of such experiments, including a comparison with the results of other techniques (Rutherford backscattering, TEM, etc.) the reader is referred to an earlier paper [20]. In this section we shall content ourselves with outlining an example where the resonances discussed in section 3.2 (see also fig. 3) have been employed in determining the thickness of the amorphous layer produced by implanting 20 keV Dy^+ ions into single crystal nickel.

Complete TCS curves for the implanted nickel are displayed in fig. 9 for a series of selected ascending sample temperatures terminating at $860°C$. These curves reveal the slow reappearance during annealing of A and B; features characteristic of the nickel crystal prior to implantation. In spite of certain experimental difficulties associated with the relative ease with which nickel oxidises there can be no doubt that the features correspond to a band structure which appears during the amorphous/crystalline transition between room temperature and $300°C$. Shifts in the surface peak also reveal the presence of at least five annealing stages in the recovery process — stages which can be readily interpreted by comparison with results obtained using other techniques [20]. Of more interest here are the clear resonances seen in fig. 9 at low energies, just above the surface peak. Following extraction of background [13] these resonances appear much sharper. Fig. 10 shows typical results for three selected temperatures. The resonances, marked by arrows, move slightly towards the "surface" (lower energies) during annealing.

Application of the analysis described by eqs. (16) to (21) is simple and direct [20]. Thus fig. 11 shows the linear fit of eq. (21) to the curves of fig. 10; resonance numbers 8–11 are involved. Corresponding layer thicknesses are 2.24, 2.33 and 2.48 nm, respectively at 310, 680 and $800°C$. The sharpness of the observed reso-
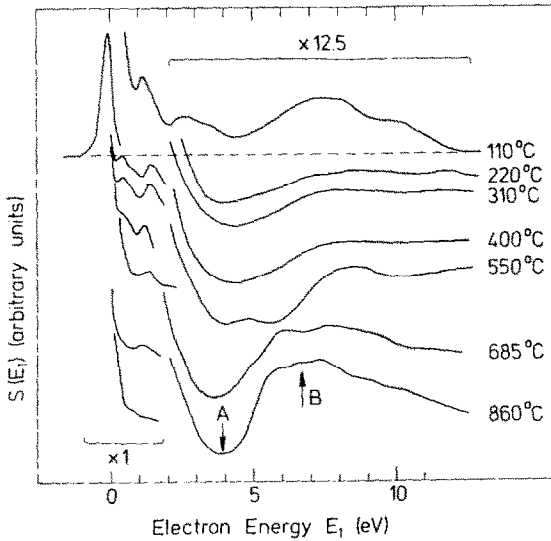
Fig. 9. Total current spectra for single crystal implanted nickel at a series of ascending temperatures. Features A and B become prominent at higher temperatures. Resonances in the low energy region gradually become less clear.

nances and their persistence to 800°C implies that there is a relatively abrupt interface at the former amorphous/crystalline boundary which continues to influence the electron scattering even after annealing at high temperatures. Two things are of note. Firstly it should be clear from fig. 11 that, within the confines of the model, TCS can be used for rather accurate measurements of the thickness of thin layers in a region where RBS, even with inclined ion beams, would be inadequate. Secondly the depth of the damaged layer as measured here by TCS is ∼2–3 nm. The most probable range of a 20 keV Dy^+ ion in a non-aligned Ni crystal, as measured by RBS, is ∼11 nm [35]. We have at present no satisfactory explanation for this discrepancy.

4.4. The band structure of molybdenite

As a final example we shall describe studies made of the scattering of electrons by good natural samples of the 2H-polymorph of the natural mineral molybdenite (2H-MoS_2) [36]. Reversible changes in typical TCS curves for molybdenite always accompanied corresponding shifts in surface potential. One such temperature-dependent family of TCS curves is shown in fig. 12, each curve displaying fine structure. For the purpose of subsequent discussion of these curves we distinguish two energy intervals. In the low energy interval, $0 < E_1 < 3.5$ eV, where E_1 is the primary electron energy above the vacuum level, there is a strong influence of tem-
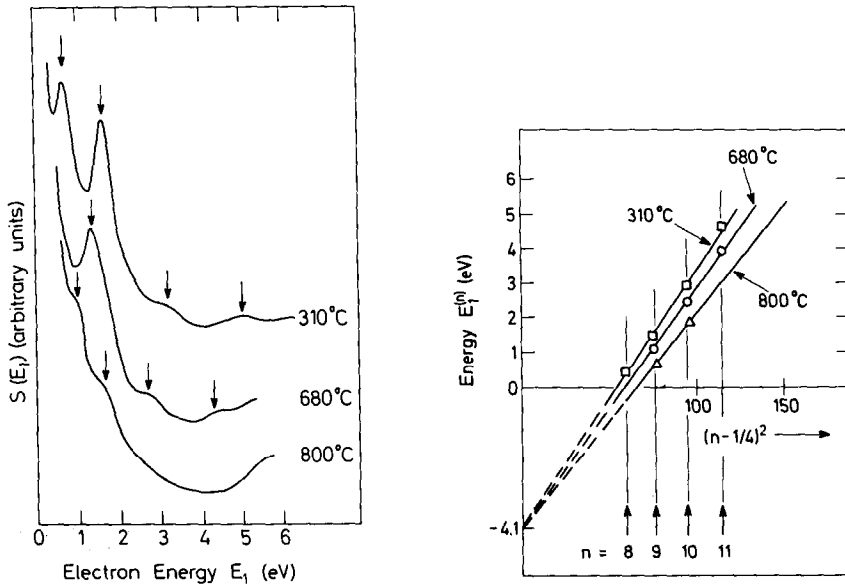
Fig. 10. Resonances in the low energy part of the TCS spectra, marked by arrows, move slightly towards the surface during annealing (see text).

Fig. 11. Resonance energy $E_1^{(n)}$ shown as a function of $(n - \frac{1}{4})^2$ for three selected temperatures. The slight change in slope indicates a slight increase in the thickness of the "damaged" layer during annealing.
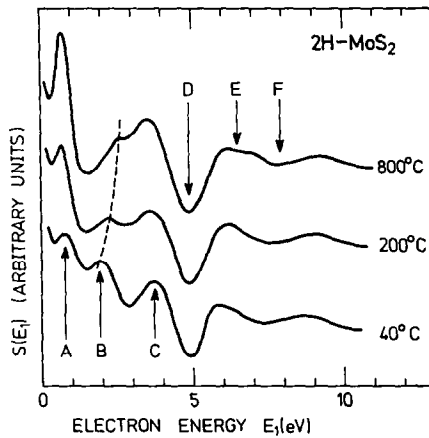

Fig. 12. Total current spectra from 2H-MoS$_2$ for selected temperatures during thermal cleaning of the surface. Structural features − marked A−D − become more prominent after gas is desorbed. The energy origin coincides with the vacuum level.

perature, and therefore of surface condition. Surface "cleaning" leads to a sharpening of the peak marked A (E_A = 1.1 eV) and a lateral drift on the energy scale of the peak marked B. The high energy interval, $E_1 > 3.5$ eV), and the troughs D, E and F (E_D = 5.0 eV, E_E = 6.7 eV and E_F = 8.0 eV).

Numerical calculations of TCS spectra for 2H-MoS$_2$ have been made on the basis of the scattering analysis outlined in section 3.1 (eqs. (9)–(15)), with two further approximations:
(i) the probability for elastic scattering is constant in the energy interval concerned,
(ii) the probability for inelastic scattering increases linearly with energy and becomes comparable with that for elastic scattering at $E_1 \simeq 8$ eV.

Mattheiss has published electronic band models for several transition-metal–dichalcogenide layer compounds [37–38] – including 2H-MoS$_2$ – and calculated using the nonrelativistic augmented-plane-wave (APW) method. For present purposes we have adopted the density of states from his 2H-MoS$_2$ band structure (fig. 13), which contains a hybridization gap within the metal $d_z{}^2$ and $d_{x^2-u^2,xy}$ manifolds. The $d_z{}^2$ is the uppermost valence band and the $d_{x^2-y^2,xy}$ the conduction band above, the width of the forbidden gap being about 1.6 eV. Below the $d_z{}^2$ band lies the valence p band of sulphur, whilst a band of empty s states is separated from the top of the conduction band by an energy gap of about 2 eV. The bottom of the s band is ~1 eV above the vacuum level. Results of the calculations are displayed in fig. 14.
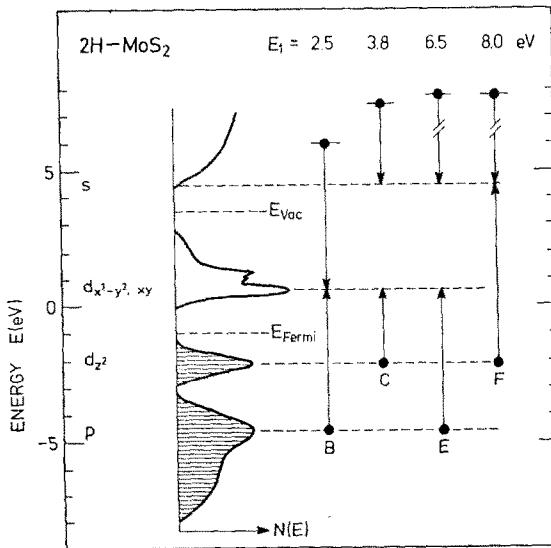

Fig. 13. Densities of states diagram for 2H-MoS$_2$ (after Mattheiss). Transitions responsible for structure in the spectra of fig. 12 are shown at the right hand side. E_{Vac} and E_{Fermi} mark the positions of the vacuum and Fermi levels respectively.
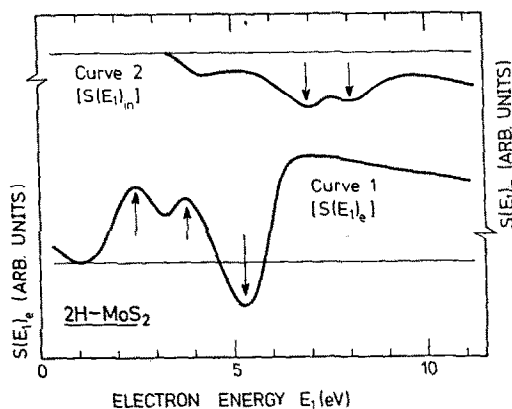
Fig. 14. Energy dependence of the elastic (curve 1) and inelastic (curve 2) contributions to the total current spectrum calculated as described in the text. Features marked by arrows should be compared with corresponding features in fig. 12 and with transitions in fig. 13.

Within the limits of approximations (i) and (ii) it follows from eq. (13) that the contribution to $S(E_1)$ from elastic scattering is a function of the energy dependence of $L(E_1)$; variations in the mean free path due to inelastic scattering affect the elastic component of the spectrum. Thus the elastic component (curve 1) has peaks at $E_1 = 2.5$ and 3.8 eV, and a broad trough at $E_1 = 5$ eV. These features are clearly associated with the energy dependence of the probability for inelastic scattering. Strong scattering probabilities arise when electron excitations take place between density of states maxima, and when the primary electrons themselves are scattered to states of high density. For $E_1 = 2.5$ eV we have the following transitions:

$$p \rightarrow d_{x^2-y^2,xy} \; ,$$

and the primary electrons fall to the sharp maximum in the empty $d_{x^2-y^2,xy}$ band. For $E_1 = 3.8$ eV we have

$$d_{z^2} \rightarrow d_{x^2-y^2,xy} \; ,$$

and the primary electrons are scattered to the bottom of the band of empty s states. These four transitions are indicated by arrows in fig. 13.

The broad trough in curve 1 (see also fig. 12) covers that range of energies for which excitation of transitions between density of states maxima accompanies primary electron scattering to the forbidden gap in the vicinity of the vacuum level. This situation is realized at primary energies ~ 5 eV.

The inelastic component (curve 2, fig. 14) is determined by the emission of electrons scattered into states above the vacuum level; an emission current increase causes a transmission current decrease which appears in the total current spectrum

as a trough. For $E_1 = 6.5$ eV we again have the transition

$$p \rightarrow d_{x^2-y^2, xy} \, ,$$

and for $E_1 = 8$ eV:

$$d_{z^2} \rightarrow s \, ,$$

in each case the primary electrons being scattered to the bottom of the s band. These two transitions are indicated by arrows in fig. 13.

From a comparison of the experimental spectra (fig. 12) with the theoretical predictions (fig. 14) we conclude that the main features of the TCS curves for 2H-MoS$_2$ are indeed due to band structure dependent details in the elastic and inelastic reflection of electrons. For $E_1 < 3.5$ eV the shape of the TCS curve is influenced only by elastic reflection. For $E_1 > 3.5$ eV both elastic and inelastic components are involved. Our simple analysis, however, does not explain the low energy peak A. One possible origin for this peak is a sharp fall in the elastic reflection coefficient near the bottom of the s band. Similar effects have been seen with nickel [2] and with copper [28], for which elements the bottom of the empty band is also situated above the vacuum level. The position of the peak B, however, is evidently dependent on the extent to which the surface is covered by adsorbed gas molecules, approaching the theoretically predicted position for cleaner conditions. Since this peak is due to electron scattering to the maximum in the $d_{x^2-y^2, xy}$ density of states, and since splitting of the d band is a direct consequence of interactions between the layers, one possible interpretation is that adsorbed surface gas can affect the basic interlayer interactions. If true this implies that total current spectroscopy will find applications in studies of intercalation [35].

The detailed band structure of 2H-MoS$_2$ has been the subject of some controversy. Many techniques [39] — including synchrotron radiation, photo-emission (both uv and X-ray photoelectron spectroscopy [40] and angular-dependent photoelectron spectroscopy), and electron energy loss measurements [41] — have been used as experimental probes. Early EPR measurements by Title and Shafer [42] were subsequently reinterpreted [43] to show that the top of the valence band has p_z character. It is now therefore generally accepted that there is strong overlap between the p_z and d_{z^2} of the valence band, at least at the Γ point. This latter could easily be missed in photoemission work. Such an assignment would also satisfy optical absorption observations. A low absorption coefficient which sets in at ~ 1.2 eV is probably due to indirect d—d transitions, whilst a stronger absorption above ~ 1.6 eV would come from indirect p—d transitions [44]. The fundamental A and B excitons above ~ 1.8 eV, for which the oscillator strengths are very large, would naturally then be associated with *direct* p—d transitions, as initially proposed by Wilson and Yoffe [45].

Finally, with respect to the conduction bands, our results are in accord with the vacuum ultraviolet reflectivity work of Hughes and Liang [46]. A reflectivity minimum in the molybdenum dichalcogenides, which is absent in the tungsten com-

pounds, marks a well defined window in the optical joint density of states, with a second region of interband transitions on the high energy side. The window in the conduction band density of states (fig. 13) is readily understood in terms of the electronic configuration of free atoms. Thus the energy separation between nd and $(n + 1)$s levels increases with decreasing principal quantum number n, so that the molybdenum 4d and 5s levels are better separated than the tungsten 5d and 6s levels. This increase naturally carries over into the corresponding band structures.

The total current spectroscopy work we have described can be satisfactorily explained on the basis of the band model of Mattheiss. It is quite obvious, however, that it is the relative positions on the energy scale of sharp maxima in the densities of states which strongly influence the spectra, and overlap of the $d_z{}^2$ and p bands [47] can readily be included without seriously affecting the positions of peaks and troughs.

5. Conclusion

A brief review has been given of the technique of Total Current Spectroscopy. In view of the difficulties involved in direct energy analysis of secondary electrons at very low energies it is surprising that the simple ploy of electronic differentiation of the target beam has not yet been more widely exploited. The spectra contain detailed information as to the physics of the surface, the near surface, and the bulk.

Acknowledgements

References

[1] J.S. Williams, Nucl. Instr. Methods 126 (1975) 205.
[2] S. Andersson and B. Kasemo, Solid State Commun. 8 (1970) 961.
[3] J. Capart, Surface Sci. 13 (1969) 361.
[4] N.P. Bazhanova, V.V. Korablev and A.A. Li, Fiz. Tverd. Tela 17 (1975) 2501.
[5] S.A. Komolov and L.T. Chadderton, Solid State Commun. 20 (1976) 765.
[6] H. Hiraska and W.H. Hamill, J. Chem. Phys. 57 (1972) 3881.
[7] T. Huang and W.H. Hamill, J. Chem. Phys. 61 (1974) 3144.
[8] V.E. Henrich, Rev. Sci. Instr. 44 (1973) 456.
[9] K. Yoto and K. Ishikawa, J. Appl. Phys. 43 (1972) 1554.

[10] J. Kirschner and P. Staib, Appl. Phys. 6 (1975) 99.
[11] P.A. Wolff, Phys. Rev. 85 (1954) 56.
[12] R.F. Willis, B. Fitton and G.S. Painter, Phys. Rev. B9 (1974) 1926.
[13] S.A. Komolov and L.T. Chadderton, Radiation Effects 31 (1976) 1.
[14] S.A. Komolov and L.T. Chadderton, Radiation Effects 81 (1976) 193.
[15] E. Bauer, J. Vacuum Sci. Technol. 7 (1970) 3.
[16] C.N. Berghund and W.E. Spicer, Phys. Rev. 136 (1964) A1030.
[17] E.O. Kane, Phys. Rev. 159 (1967) A624.
[18] D.E. Eastman, Solid State 8 (1970) 41.
[19] R.W. Strayer, W. Mackie and L.W. Swanson, Surface Sci. 34 (1973) 225.
[20] L.T. Chadderton, E. Johnson and S.A. Komolov, Nucl. Instr. Methods 149 (1978) 639.
[21] J.W. Gadzuk, Surface Sci. 18 (1969) 193.
[22] G.M.K. Watts, Surface Sci. 23 (1970) 453.
[23] S. Andersson and B. Kasemo, Surface Sci. 32 (1972) 78.
[24] L. Fiermans and J. Vennik, Surface Sci. 35 (1973) 42.
[25] P.A. Anderson, Phys. Rev. 59 (1941) 1034.
[26] L. Fiermans and J. Vennik, Phys. Status Solidi 41 (1970) 621.
[27] D.E. Eastman, Solid State Commun. 7 (1969) 1697.
[28] E.G. McRae and C.W. Caldwell, Surface Sci. 57 (1976) 63.
[29] H. Kanter, Phys. Rev. B1 (1970) 522.
[30] W.F. Krowlikowski and W.L. Spicer, Phys. Rev. 185 (1969) 882.
[31] L.T. Chadderton and M.G. Anderson, Thin Films 1 (1968) 229.
[32] J.C. Mitchinson and R.D. Pringle, Appl. Phys. Letters A (1970) 326.
[33] V.I. Vladimirov, Soviet Phys. Solid State 7 (1965) 1536.
[34] R.D. Gretz, J. Phys. Chem. Solids 27 (1966) 1849.
[35] R. Andrew, Phil. Mag. 35 (1977) 1153.
[36] S.A. Komolov and L.T. Chadderton, Phil. Mag. 39 (1979) 13.
[37] L.F. Mattheiss, Phys. Rev. Letters 30, (1973) 784.
[38] L.F. Mattheiss, Phys. Rev. B8 (1973) 3719.
[39] A.D. Yoffe, Chem. Soc. Rev. 5 (1976) 51.
[40] J.C. McMenamin and W.E. Spicer, Phys. Rev. Letters 29 (1972) 1501.
[41] M.G. Bell and W.Y. Liang, Advan. Phys. 25 (1976) 53.
[42] R.S. Title and M.W. Shafer, Phys. Rev. Letters 28 (1972) 808.
[43] F. Mehran, R.S. Title and M.W. Shafer, Solid State Commun. 20 (1976) 368.
[44] A.M. Goldberg, A.R. Beal, F.A. Levy and E.A. Davies, Phil. Mag. 32 (1975) 367.
[45] J.A. Wilson and A.D. Yoffe, Advan. Phys. 18 (1969) 193.
[46] H.P. Hughes and W.Y. Liang, J. Phys. C7 (1974) 1023.
[47] J.C. McMenamin and W.E. Spicer, Phys. Rev. 16 (1977) 5475.